FY2013 Theory Milestone
Third Quarterly Report
June 27, 2013

Submitted by: S. C. Jardin, PPPL jardin@pppl.gov

I. Introduction and Outline

The FY2013 Theory Target on Disruption Physics consists of two major topics which we will refer to as "disruption forces" and "runaway electron confinement during MGI".   Both of these have several sub-topics. The Q1 quarterly report concerned only disruption forces, and the Q2 report concerned only runaway electron confinement during MGI.   The original plan was to continue this separation with the Q3 and Q4 reports each being a report on only one of these two topics.

However, because substantial progress has been made in each of these two topics since the previous reports, and also because the analysis for both topics is still ongoing, our team, in consultation with John Mandrekas of the OFES, has decided to make this Third Quarterly Report a progress report on both the original Q3 and Q4 milestones, as listed in the Appendix, and to follow this up with a final Q4 report by September 30 2013 in which we will present the final analysis of both topics.

II. Calculation of Disruption Forces

A. ITER Disruption Modeling

In the simulations presented in this section, we used a poloidal computational mesh with 43,200 points and 32 toroidal planes.   This is a total of 1,382,400 mesh points.   This mesh is 2^3 times larger than those used in the previous ITER simulations reported in Q1.   This increased resolution allows the use of more realistic parameters.   In particular, the Lundquist number is now S = 10^6, and the wall time is now much greater than the Alfven time, $\tau_{wall} \geq 10^3 \tau_A$.

There are 3 relevant time scales in a disruption. The first is the resistive wall penetration time, τ_{wall} , which determines the vertical displacement event (VDE) growth time. The VDE scrapes off magnetic flux, causing the safety factor, q, at the last closed flux surface to drop to $q \cong 2$, causing the plasma to become ideal MHD unstable.

The second time scale is the growth time of the $n=1$ modes, denoted by γ^{-1} .   These modes, predominantly $(2,1)$ and $(1,1)$, cause the magnetic field to become stochastic, producing the thermal quench (TQ) which drastically cools the plasma in a very short time and initiates the current quench. Hence: $\tau_{TQ} = \gamma^{-1} \simeq 10^2 \tau_A$.

The third timescale is the halo region resistive time, which we denote by τ_{halo} The TQ cools the plasma to the halo temperature, causing the plasma current to resistively decay in time τ_{halo} . In addition, the plasma current is carried into (or scraped off by) the wall by the VDE, which also contributes to the

current quench (CQ). Thus, $\tau_{CQ} = \min(\tau_{halo}, \tau_{wall})$. Note that the resistive time of the pre-thermal quench plasma, $\tau_r = S \tau_A$ is not important, as long as it is large enough not to have much effect on γ.

Let us now discuss the $\gamma \tau_{wall}$ scaling. In previous work [1], we found the asymmetric wall force was a maximum when $\gamma \tau_{wall} \simeq 1$. In that case, if $\tau_{wall} \simeq \tau_{halo}$, it implies that the thermal quench and the current quench occur on the same timescale, $\tau_{TQ} \simeq \tau_{CQ}$. (Note that $\gamma \approx 0.01 \tau_A^{-1}$)
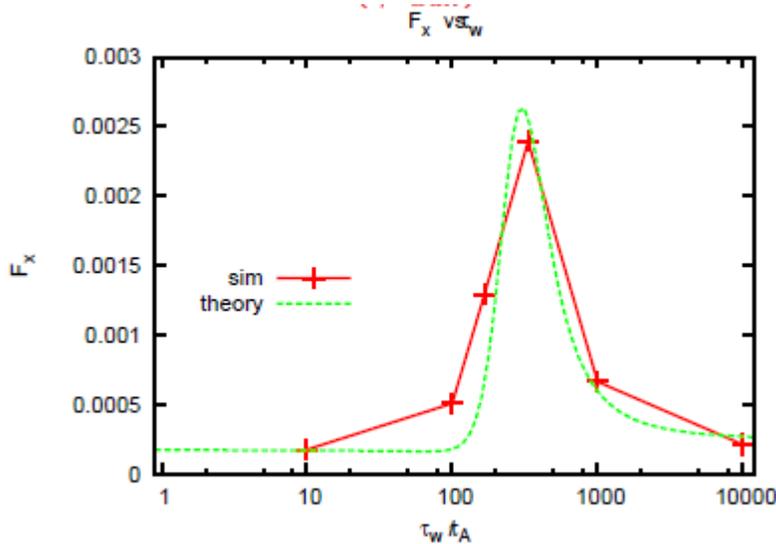

Figure 1: Previous calculations showed the relation between the asymmetric wall force and the wall time.

The reason for this dependence was explained in Ref. [1]. For $\gamma \tau_{wall} \gg 1$, the asymmetric force is much smaller. In order for the thermal quench time to be much shorter than the current quench time, $\tau_{TQ} \ll \tau_{CQ}$, as is normally observed in experiments, we need $\gamma^{-1} \ll \min\left(\tau_{wall}, \tau_{halo}\right)$ such as depicted in Figure 2.
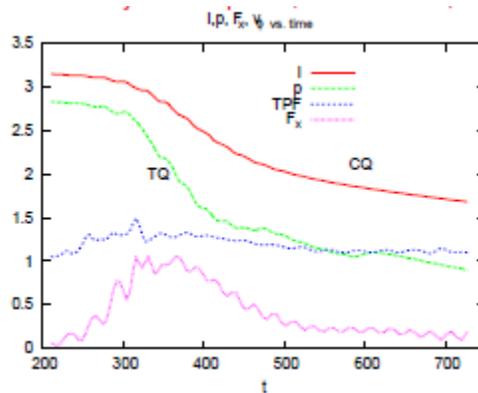

Figure 2: Time history of disruption. (This figure is an example which was previously performed with lower resolution than the milestone results being presented here)

Shown in Figure 2 are normalized total current I, the normalized total pressure p and the toroidal peaking factor denoted TPF. Also shown is F_x, the dimensionless sideways wall force multiplied by 10^4. The maximum value of F_x in this calculation was only about 3% of the maximum F_x that can be tolerated by ITER. The force was so low in this calculation because $\gamma \tau_{wall}$ is greater than rightmost point on Fugure 1 of F_x vs $\gamma \tau_A$.
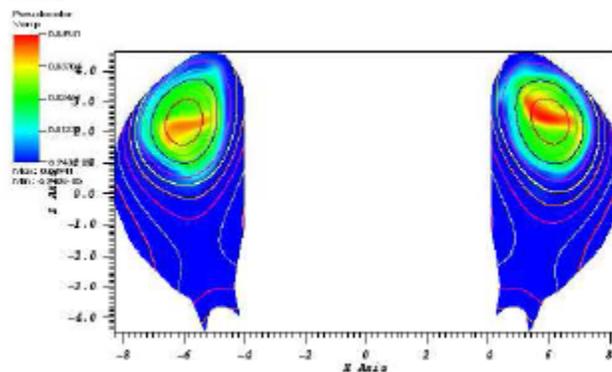

Figure 3 Contour plot of *p(R,Z,π)*, *p(R,Z,0)* at time t = 754.9 τ_A dominated by (2,1) mode.
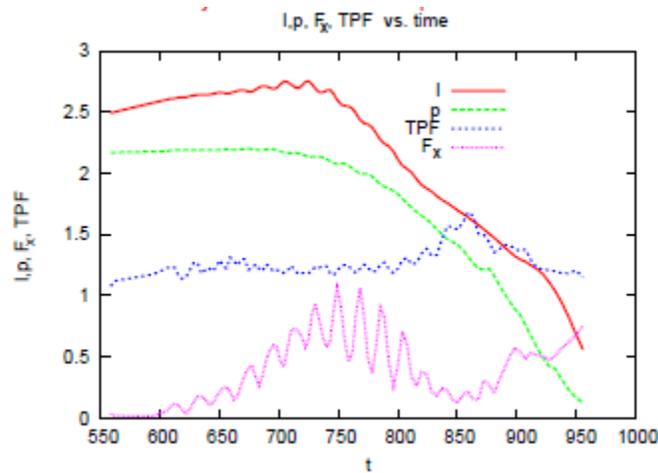

Figure 4: Time history of milestone simulation

Figure 3 shows a snapshot of the pressure contours of one of the new high resolution simulations. In Figure 4, we show some traces for the time history of the simulation shown in Figure 3. Shown are normalized total current I, normalized total pressure p, and TPF. Also shown is F_x, the dimensionless sideways wall force multiplied by 10^4. Here again, the maximum value of F_x in the calculation is only 3% of that which can be tolerated by ITER, similar to the result found in the lower resolution case above. The time history differs from the non milestone case, because the VDE evolution was somewhat

different, giving a mode with smaller growth rate γ. The increase of the plasma current I is caused by a modification of the resistivity profile in the initial stage of run.

In the above simulation, $\tau_{wall} \gg \tau_{halo}$ but $\gamma\,\tau_{halo} \sim 1$. Hence, $\gamma\,\tau_{wall} \gg 1$, producing a relatively small asymmetric wall force, but also having the thermal quench time and current quench times comparable, $\tau_{TQ} \approx \tau_{CQ}$. A simulation is presently in progress with longer τ_{halo}, which should produce a more physically relevant disruption sequence with $\tau_{TQ} \ll \tau_{CQ}$. This will be presented in the Q4 progress report.

B. NSTX disruption modeling

The parameters used in the new Q3 milestone runs for NSTX have been greatly expanded over those used in the Q1 milestone runs, allowing a much larger separation of time scales, and thus increased realism. In the new runs, the duration of the VDE phase is now effectively 70,000 τ_A (seven wall times) This was made possible by performing this part of the calculation, where the plasma was only unstable to a n=0 mode, in 2D rather than in 3D. When the thermal quench begins, the n=1 mode is now predominantly m=1. In these runs, the confinement is destroyed by the thermal quench before current quench sets in, much more like what is observed in experiments. We also observe that the total plasma current, I_p, rises slightly before collapsing in quench phase, as is typically observed in experiments. The peak vertical force is somewhat smaller in the new runs, whereas the ratio of peak horizontal to vertical forces is similar. Table 1 presents a comparison of the parameters used in the Q1 report and those used in the present calculations, which will be presented in more detail in the upcoming Q4 report.

Table 1: Parameter comparison, Q1 vs Q3

	1st quarter	3rd quarter
Number of radial zones	111	115
Number of toroidal planes	18 (6 toroidal modes)	40 (13 toroidal modes)
Total vertices	671,346	1,600,840
Central plasma resistivity η_0	5×10^{-6}	5×10^{-8}
Wall resistivity η_w	2.25×10^{-2}	10^{-4} ($\tau_w \sim 10$ ms)
"Vacuum" resistivity η_v	6×10^{-2}	1.67×10^{-4}
Perp. heat diffusion $\kappa_\perp$	10^{-5}	10^{-5}
Parallel heat diffusion $\kappa_{\|\|}$	Artificial sound; $v_{Te}=2v_A$	10^{-1}

III. The effect of spatially non-symmetric source terms on runaway electron confinement

In the second quarter milestone we reported on runaway electron (RE) losses in simulations of Ar-pellet-like uniform impurity injection compared with Ne-MGI-like injection which was toroidally uniform, but poloidally localized to the low-field-side (LFS) edge. Here we report initial observations from four further simulations of Ne MGI in which the impurity source is also toroidally localized, with more detailed analysis to follow in the Q4 report.

A. Description of toroidally-localized MGI sources

In two of the four simulations, the impurity source has the same poloidal distribution as the previous toroidally symmetric case—radially localized to the edge and poloidally peaked on the LFS. The other two simulations have the Ne source poloidally peaked on t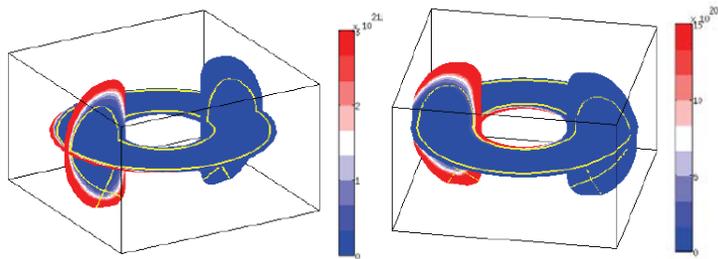he high-field-side (HFS) with the same radial profile. The two LFS simulations (and the two HFS simulations) are differentiated from one another by the degree of toroidal peaking of the source. In one LFS (and one HFS) case, the Ne source is spread about 2/3 of the way around toroidally; the other cases are more toroidally peaked, with the impurities spread about 1/3 of the way around. Two examples of injection sources, showing both the variation in poloidal and in toroidal distribution, are plotted in Figure 5.

Figure 5. (Left) 3D contour plot of Ne source distribution (Ne density in m^{-3}) for LFS injection with 1/3 toroidal spreading of impurities. (Right) Ne source distribution for HFS injection with 2/3 toroidal spreading of impurities.

B. Comparison of RE losses

Figure 6 shows both the n=1 mode amplitude and the fraction of RE losses for the two simulations presented in the Q2 milestone and the four additional toroidally peaked simulations. First, the RE losses are seen to occur earlier in all toroidally peaked simulations than in those with toroidally symmetric impurities. In the toroidally symmetric cases, the n=1 amplitude grows from the noise after the n=1 mode becomes unstable. In the toroidally peaked cases, the gas injection itself represents a significant n=1
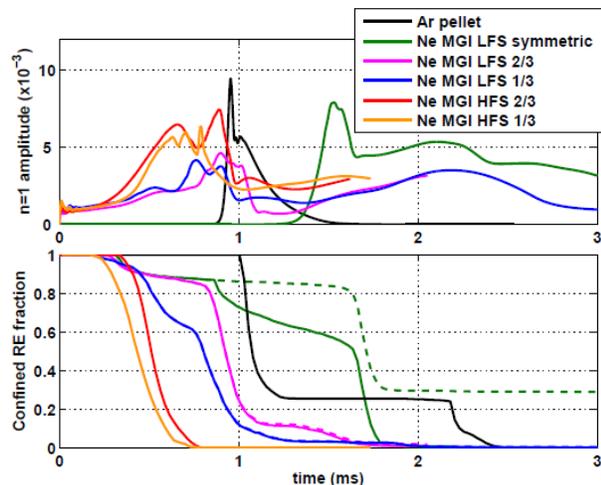

Figure 6. (Top) Amplitude of the n=1 mode for six simulations. (Bottom) Confined fraction of REs versus time for six simulations.

perturbation, which can be seen beginning at t=0.   Consequently, the n=1 mode grows and saturates earlier, particularly compared to the symmetric MGI case.

A second notable feature of these results is that, for both the LFS and HFS injection cases, the more toroidally peaked source of each pair produces earlier RE losses than the case with broader toroidal peaking. Although this appears linked to earlier n=1 mode saturation in the LFS injection simulations, this is not the case for HFS injection. The third clear trend in this set of simulations is the overall earlier loss of REs in the HFS simulations. In fact, the HFS RE losses clearly precede the n=1 mode growth and saturation, which is unique among all of the simulations. This and the previous observation point to the possibility that the imposed perturbation from a non-symmetric jet may have a direct de-confining effect on some fraction of REs, independent of any unstable mode growth. And, in particular, this effect is more pronounced for HFS than for LFS injection, and also for a more toroidally localized source. In the Q4 report we will examine more closely the evolution of field-line topology for each of these cases, and the effect on individual RE orbits, particularly to understand the early RE loss in the HFS injection cases. Little data on HFS MGI exists—although ASDEX results indicated better fueling efficiency from the HFS [2]—and none on its effects on RE confinement, but these data may point to a second beneficial feature of injection from the HFS.

IV. Summary

Considerable progress has been made in each of the two major topics since the Q1 and Q2 milestone reports.   The 2013 Theory Target is concerned with predicting disruption forces and runaway electron confinement.   The progress made in predicting disruption forces since the Q1 milestone report has been made possible by our ability to use the massively parallel computer Hopper at NERSC to increase the total number of mesh points in our calculation by a factor of 8.   This higher resolution, and our continuing better understanding of the role of different physical parameters in producing disruption forces has allowed a much more realistic disruption simulation to be performed.   The Q4 milestone will present the completion of these simulations and draw conclusions from them as well.

In the area of runaway electron confinement, the work presented here extends that described in the Q2 milestone report, primarily by removing the toroidal symmetry that we previously imposed on the MGI sources.   This is much more realistic in modeling the experimental configurations.   The Q4 milestone will present additional analysis of the role of source symmetry in affecting the outcome.

References:

[1] H. Strauss, R. Paccagnella, J. Breslau, L. Sugiyama, S. Jardin, "Sideways wall force produced during tokamak disruptions", Nuclear Fusion 53, 073018 (2013)

[2] G. Pautasso, et. al. "Massive gas injection from the high field side of ASDEX Upgrade," *Proceedings of the 38th EPS Conference on Plasma Physics*, Strasbourg (2011).

Acknowledgements:

Appendix: FY 2013 Theory Target on Disruption Physics:

Carry out advanced simulations to address two of the most problematic consequences of major disruptions in tokamaks: the generation and subsequent loss of high-energy electrons (runaway electrons), which can damage the first wall, and the generation of large electromagnetic loads induced by disruptions, and assess the severity of these effects on ITER

Original Quarterly Milestones:

Q1. Perform a 3D MHD simulation of a vertical displacement event (VDE) disruption at twice the resolution and wall time constant of previous studies to determine the scaling of the 3D forces on the axisymmetric conducting structures, and how these forces differ from those obtained in 2D calculations.

Q2. Perform a 3D MHD simulation of a DIII-D mitigated disruption experiment with symmetric impurity source terms to determine the effects of the source terms and MHD activity on test-particle runaway electron confinement.

Q3. Extend the 3D MHD simulations of VDEs to higher resolution by again doubling the grid resolution and increasing the simulation time period from that used in Q1. This will allow an increase in the Lundquist number to $S=10^6$ and a further doubling of the wall time-constant.

Q4. Extend the simulations of the DIII-D mitigated disruptions to model the effect of spatially non-symmetric source terms on runaway electron confinement.